ADVANCED HEALTHCARE MATERIALS
www.advhealthmat.de

Biomimetic Multilayered Gas-Foaming Scaffold with Sustained bFGF Delivery for Annulus Fibrosus Regeneration

Yujie Chen, Yucai Li, Zhenyuan Wei, Lin Du, Mingyang Qian, Jielin Wang, Xiumei Mo, Zijun Deng,* Xiaojian Ye,* and Jiangming Yu**

Current clinical treatments for intervertebral disc (IVD) herniation (e.g., discectomy) often lead to re-herniation, and tissue engineering scaffolds for annulus fibrosus (AF) regeneration remain scarce, particularly those capable of mimicking the multilayered structure of native AF. This study combines electrospinning with gas-foaming technology to fabricate a 3D nanofiber scaffold (3DS) with a hierarchical multilayered structure. Subsequently, fibronectin is employed as a "bridge" to immobilize basic fibroblast growth factor (bFGF) onto 3DS through its inherent gelatin and heparin binding domains, ultimately constructing a 3D bioactive AF scaffold (3DFF). In vitro experiments demonstrate that the 3DFF mimicks the multilayered structure of native AF. Through sustained bFGF release, it enhances extracellular signal-regulated kinase (ERK) phosphorylation and activates the Wnt/β-catenin pathway, thereby promoting cell proliferation, migration, and matrix secretion. In vivo experiments using a rat tail AF defect model show that 3DFF mitigates IVD degeneration and facilitates AF regeneration. In summary, this study develops a bioactive biomimetic multilayered annulus fibrosus scaffold, offering a promising strategy for annulus fibrosus repair following discectomy.

1. Introduction

The global rise in aging populations has brought increased attention to intervertebral disc (IVD) degeneration, a prevalent health issue often leading to back pain.[1] This degeneration can cause nucleus pulposus (NP) extrusion through tears in the annulus fibrosus (AF), compressing nerve roots or the spinal cord and resulting in severe pain and neurological disorders.[2] Current conservative treatments for disc herniation, such as non-steroidal anti-inflammatory drugs, acupuncture, and massage, often prove insufficient in severe cases, necessitating disc excision surgery.[3] Unfortunately, this surgery carries a risk of complications, including compromised AF structure and recurrent disc herniation, affecting a significant percentage of patients.[4–6] Existing repair methods, like AF suturing or closure device insertion, fail to adequately regenerate damaged tissues, leading to suboptimal long-term outcomes.[7,8] Therefore, developing effective AF scaffolds for IVD repair is crucial.

Tissue engineering applies principles of engineering and life sciences to develop biological substitutes, providing a new therapeutic strategy for AF repair.[9] The natural AF is located at the periphery of NP tissue, where the cells mainly consist of fibroblasts distributed in concentric layers of the annulus. Therefore, the concentric nanofiber structure is a key factor in the design of AF tissue engineering scaffolds. Electrospinning, a versatile nanofiber fabrication technique, is applicable to a wide range of materials.[10] However, conventional electrospun nanofibrous membranes have a dense structure, hindering cell infiltration and nutrient transport. Gas foaming, a post-processing technique, has emerged as a promising approach for constructing 3D nanofibrous scaffolds for tissue engineering.[11] This technique offers several advantages over other methods, including high efficiency, simplicity, and the ability to fabricate integrated and continuous multilayered structures. Notably, these multilayered nanofibrous scaffolds can mimic the natural lamellar architecture of the AF. Recent studies have demonstrated the efficacy of gas-foamed 3D nanofibrous scaffolds in supporting cell and tissue growth.[12,13] However, the application of this technology for AF tissue engineering remains largely unexplored, particularly regarding the enhancement of scaffold bioactivity to promote cell recruitment and maintain normal AF function.

Y. Chen, Y. Li, Z. Wei, L. Du, M. Qian, J. Wang, X. Ye, J. Yu
Shanghai Key Laboratory of Flexible Medical Robotics
Tongren Hospital
Institute of Medical Robotics
Shanghai Jiao Tong University
1111 XianXia Road, Shanghai 200336, China
E-mail: 732004380@shsmu.edu.cn; 732004381@shsmu.edu.cn
X. Mo
Institute of Biomaterials and Biomedicine
School of Food and Pharmacy
Shanghai Zhongqiao Vocational and Technical University
3888 Caolong Road, Shanghai 201514, China
E-mail: xmm@dhu.edu.cn
Y. Chen, Y. Li, Z. Wei, L. Du, M. Qian, J. Wang, X. Ye, J. Yu
Center of Research in Minimally Invasive Spine Surgery
Department of Orthopaedics
Tongren Hospital
Shanghai Jiao Tong University School of Medicine
1111 XianXia Road, Shanghai 200336, China
Z. Deng
Hongqiao International Institute of Medicine
Tongren Hospital
Shanghai Jiao Tong University School of Medicine
1111 XianXia Road, Shanghai 200336, China
E-mail: dengzijun@shsmu.edu.cn
The ORCID identification number(s) for the author(s) of this article can be found under https://doi.org/10.1002/adhm.202502833

DOI: 10.1002/adhm.202502833

Endogenous progenitor and stem cells reside within the cartilage endplate, AF, and NP of IVD.[14] This presence suggests a promising therapeutic approach for IVD degeneration: activating resident cells to initiate repair at the injury site. However, the hostile microenvironment of the damaged tissue hinders endogenous repair by impeding the survival and differentiation of cells.[15] Therefore, creating a favorable microenvironment that supports the recruitment, viability, and differentiation of endogenous annulus fibrosus cells (AFCs) or progenitor/stem cells is essential for successful AF tissue regeneration.[16] Basic fibroblast growth factor (bFGF) demonstrates potent chemotactic properties. It can stimulate AFCs proliferation and enhance the synthesis of crucial extracellular matrix (ECM) components, including type I collagen (COL I), type II collagen (COL II) and proteoglycans, which are vital for maintaining AF structure and function. However, the clinical application of growth factors like bFGF is limited by inherent drawbacks such as instability, short half-life, rapid inactivation under physiological conditions and susceptibility to degradation.[17]

In this study, we developed a biomimetic 3D nanofiber scaffold by combining electrospinning with gas-foaming to create a multilayered architecture that replicated the lamellar organization of native AF tissue. Poly(ϵ-caprolactone) (PCL) provided tunable mechanical strength, while gelatin offered bioactive sites for cell adhesion and ECM protein binding.[18] Gelatin modification also enhanced mechanical stability without compromising structural integrity. To confer sustained growth factor delivery, we immobilized fibronectin (Fn) onto the gelatin domains, leveraging Fn's gelatin-binding region for scaffold anchorage and its heparin-binding domain for bFGF loading.[19,20] This dual functionality mitigated burst release by relying on electrostatic interactions and ECM-based anchoring, thus ensuring prolonged bFGF availability and supporting cellular infiltration throughout the scaffold (**Figure 1**).

2. Result

2.1. Fabrication and Characterization of Scaffolds

Initially, a nanofibrous membrane was fabricated utilizing electrospinning. This membrane was subsequently subjected to a gas foaming process, yielding a multilayered, 3D nanofiber scaffold. To augment the mechanical properties of the scaffold, gelatin modification was implemented. Thereafter, the scaffold was functionalized with Fn. The Fn was immobilized on the gelatin surface and interacted with bFGF through electrostatic interactions mediated by its heparin-binding domain. It was hypothesized that the multilayered architecture of the 3DFF scaffold facilitated cell and tissue infiltration, providing sufficient space for cell adhesion and ECM secretion. The controlled release of bFGF from the scaffold was anticipated to promote cellular recruitment to the defect area, stimulated cell proliferation, and expedited the repair of AF injuries.

SEM images revealed a multilayered nanofiber structure for all 3D scaffolds (**Figure 2A**). The images also illustrated the distribution of modified gelatin, appearing either as a layer on the fibers or as a network on the mat surface. No significant difference in gap distance was observed among the scaffolds, with values of 65 ± 22, 70 ± 17, and 69 ± 19 µm for 3DS, 3DF, and 3DFF, respectively (Figure 2B). Similarly, all scaffolds exhibited comparable porosity exceeding 70% (Figure 2C). Compression tests were conducted to evaluate the mechanical properties of the scaffolds. Figure 2D illustrates the elasticity of the 3DFF scaffold, demonstrating its ability to rebound smoothly to its original shape after compression. The stress–strain curves of the scaffolds at 50% deformation revealed compressive moduli of 9.08 ± 0.42, 9.92 ± 0.68, and 10.46 ± 0.85 kPa for 3DS, 3DF, and 3DFF, respectively (Figure 2E,F). The tensile stress–strain curves indicated that each scaffold exhibited comparable mechanical behavior (Figure S1A, Supporting Information). The Young's moduli of the 3DS, 3DF, and 3DFF groups were 118 ± 5 MPa, 122 ± 5 MPa, and 127 ± 7 kPa, respectively, while displaying similar tensile strengths (approximately 28 kPa) and elongations at break (around 22%) (Figure S1B—D, Supporting Information). These findings were consistent with the compression test data, confirming that the scaffold can withstand tensile loads and was suitable for annulus fibrosus repair.

FTIR spectroscopy was employed to analyze the functional groups present in the different scaffolds (Figure 2G). All scaffolds displayed characteristic peaks of PCL, including a carbonyl stretching vibration peak at 1726 cm^{-1}. The peaks at 2945 cm^{-1} and 2866 cm^{-1} corresponded to asymmetric and symmetric —CH_2— stretching vibrations, respectively. Asymmetric and symmetric C—O—C stretching vibrations were observed at 1240 cm^{-1} and 1170 cm^{-1}, respectively. Notably, after gelatin modification, two distinct peaks emerged near 1647 cm^{-1} and 1540 cm^{-1} in all 3D scaffolds. These peaks were attributed to the C = O stretching of amide I and the combined bending and stretching of N—H and C—H in amide II of gelatin. The release kinetics of bFGF from 3DFF, as depicted in Figure 2H, demonstrated an initial burst release of 45.27% on day 1, followed by a gradual increase to 56.60% by day 3. By day 12, the cumulative release reached 84.52%, highlighting the sustained release profile of bFGF from the 3DFF scaffold.

Live/dead staining assays indicated negligible cytotoxicity across all scaffold typologies (**Figure 3A**). DAPI/F-actin staining further demonstrated that the sustained release of bFGF from the 3DFF scaffold effectively preserved the fibroblastic phenotype of the AFCs (Figure 3B). Transwell migration assays indicated enhanced cell migration in the 3DFF group compared to the 3DS, 3DF, and control groups (Figure 3C,E). The fluorescence staining of DAPI/F-actin confirmed that after 3 d of culture, AFCs were able to infiltrate the interior of the 3DFF scaffold and exhibited a stereoscopic morphology (Figure 3D). The intricate architecture of the 3D scaffold facilitates multidirectional cell spreading. Multiple studies have demonstrated that various cell types, including fibroblasts, tend to adopt rounded, stereoscopic morphological characteristics in response to the 3D microenvironment.[21–23] Moreover, CCK-8 assays showed no significant difference in the proliferation of AFCs during the initial 24 h culture period, which was consistent with the live/dead staining results. However, by day 3 and day 5, the 3DFF scaffold group demonstrated a significantly higher AFCs population compared to both the control group and other scaffold groups (Figure 3F). Collectively, these findings suggested that AFCs

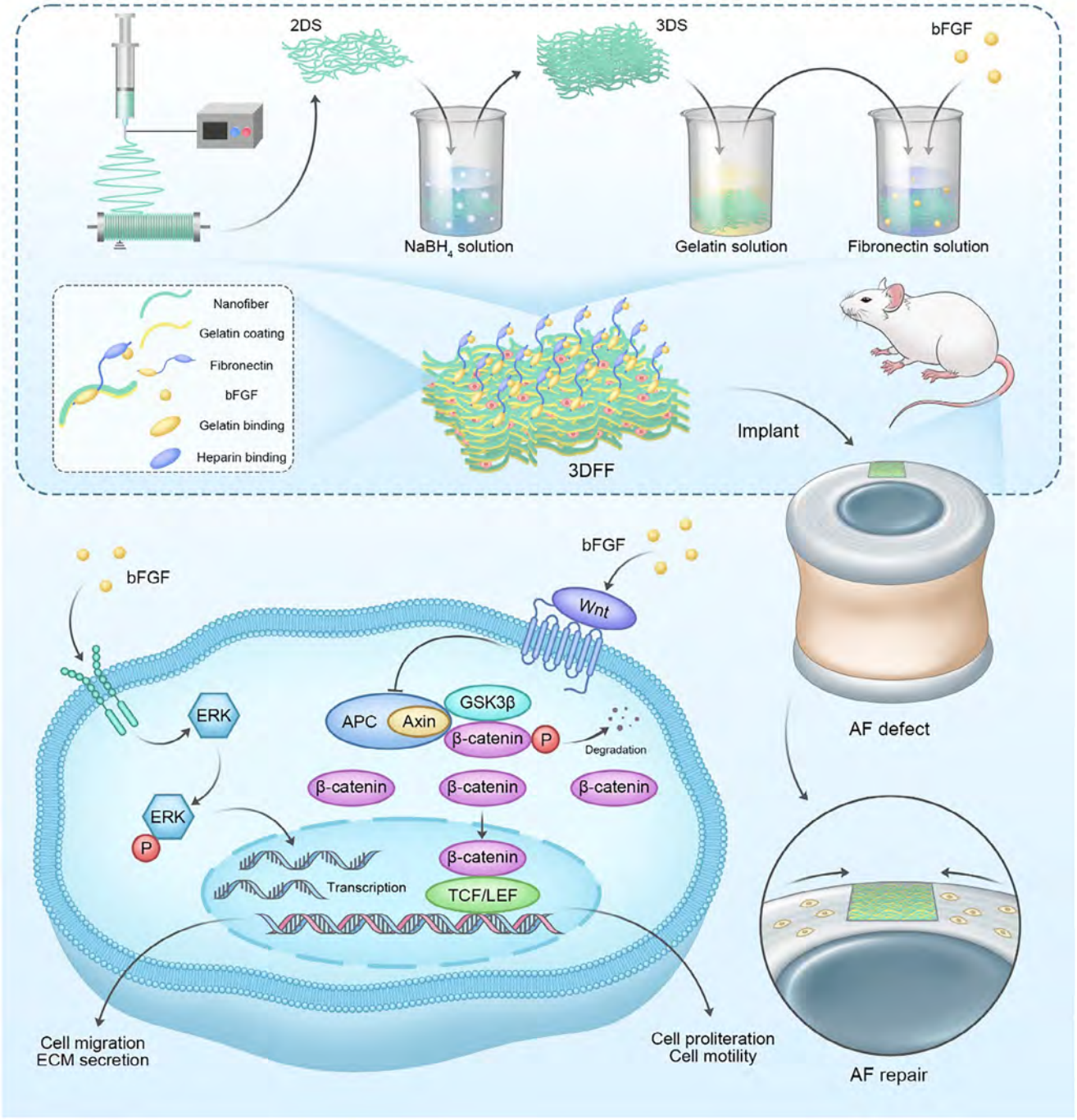

Figure 1. Schematic diagram depicting the fabrication process of 3DFF via electrospinning, gas foaming, and biofunctionalization.

not only exhibited viability but also actively infiltrated the nanofibrous architecture of the 3D scaffolds. Critically, the 3DFF scaffold, by virtue of its sustained bFGF release, exhibited a marked improvement in both AFCs migration and proliferation.

After 5 d of co-culture with scaffold extracts, AFCs were immunostained to evaluate matrix secretion. AFCs co-cultured with the 3DFF group exhibited significantly higher fluorescence intensity of COL I and ACAN, and displayed a characteristic spindle-shaped morphology (**Figure** 4A–D). This enhanced matrix production was further confirmed by qPCR, which showed significantly higher mRNA expression of COL I, COL II, and ACAN in the 3DFF group compared to the control and other scaffold groups (Figure 4E–G). Similarly, Western blot analysis demonstrated that these matrix-related protein expressions were elevated in the 3DFF group, along with increased phosphorylation levels of ERK (Figure 4H–L). These findings suggested that the 3DFF groups effectively promoted

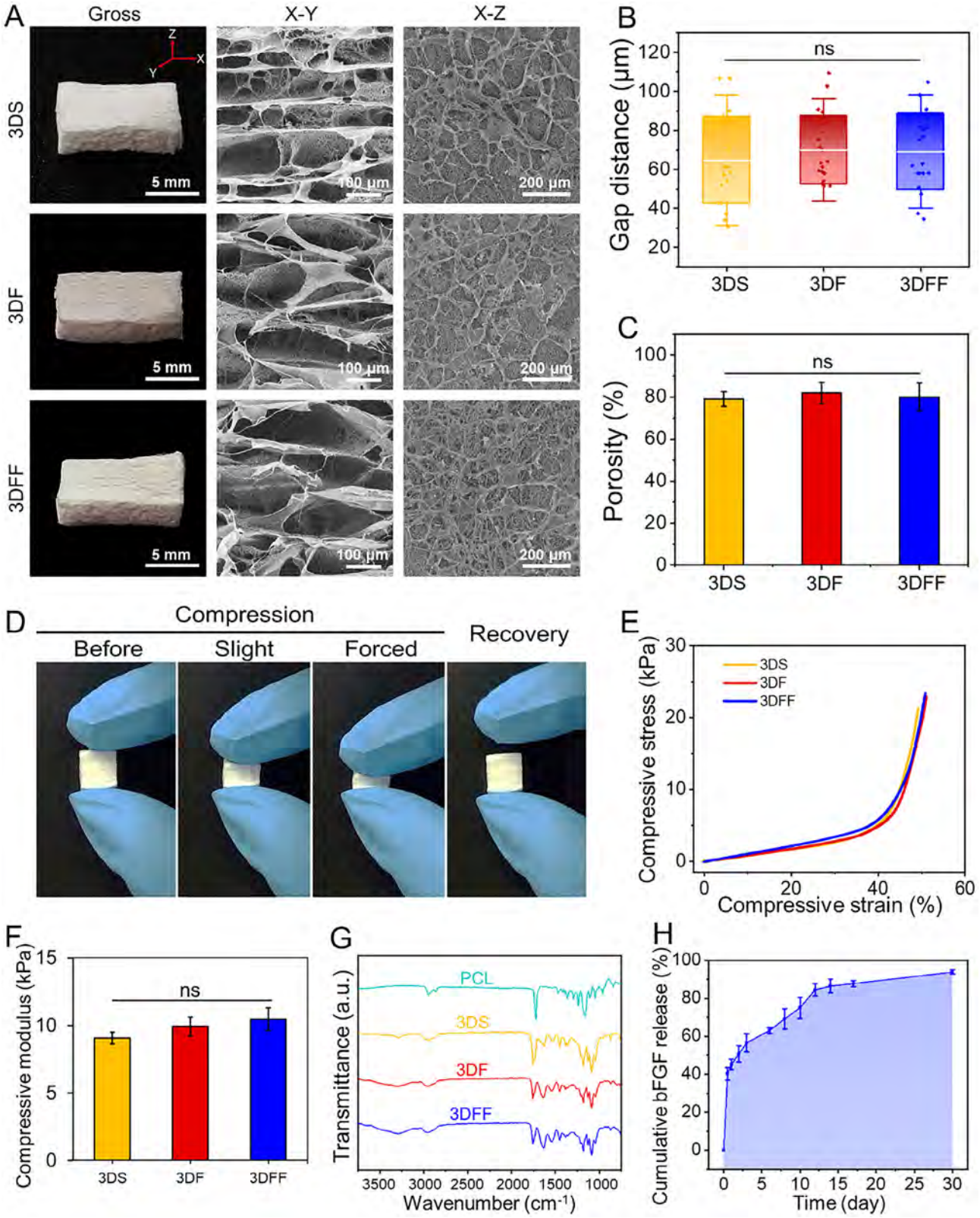

Figure 2. Physicochemical and mechanical properties of 3DS, 3DF and 3DFF. A) SEM images of 3DS, 3DF, and 3DFF scaffolds. B) Gap distance and C) porosity of the scaffolds. Mechanical properties including the compression image of D) 3DFF, E) representative stress–strain curves, and F) compressive modulus of the scaffolds ($n = 3$) G) FTIR spectra of the scaffolds. H) Release behavior of bFGF from 3DFF in PBS ($n = 3$). (#, $ indicate $p < 0.05$ compared to 3DS and 3DF, respectively.).

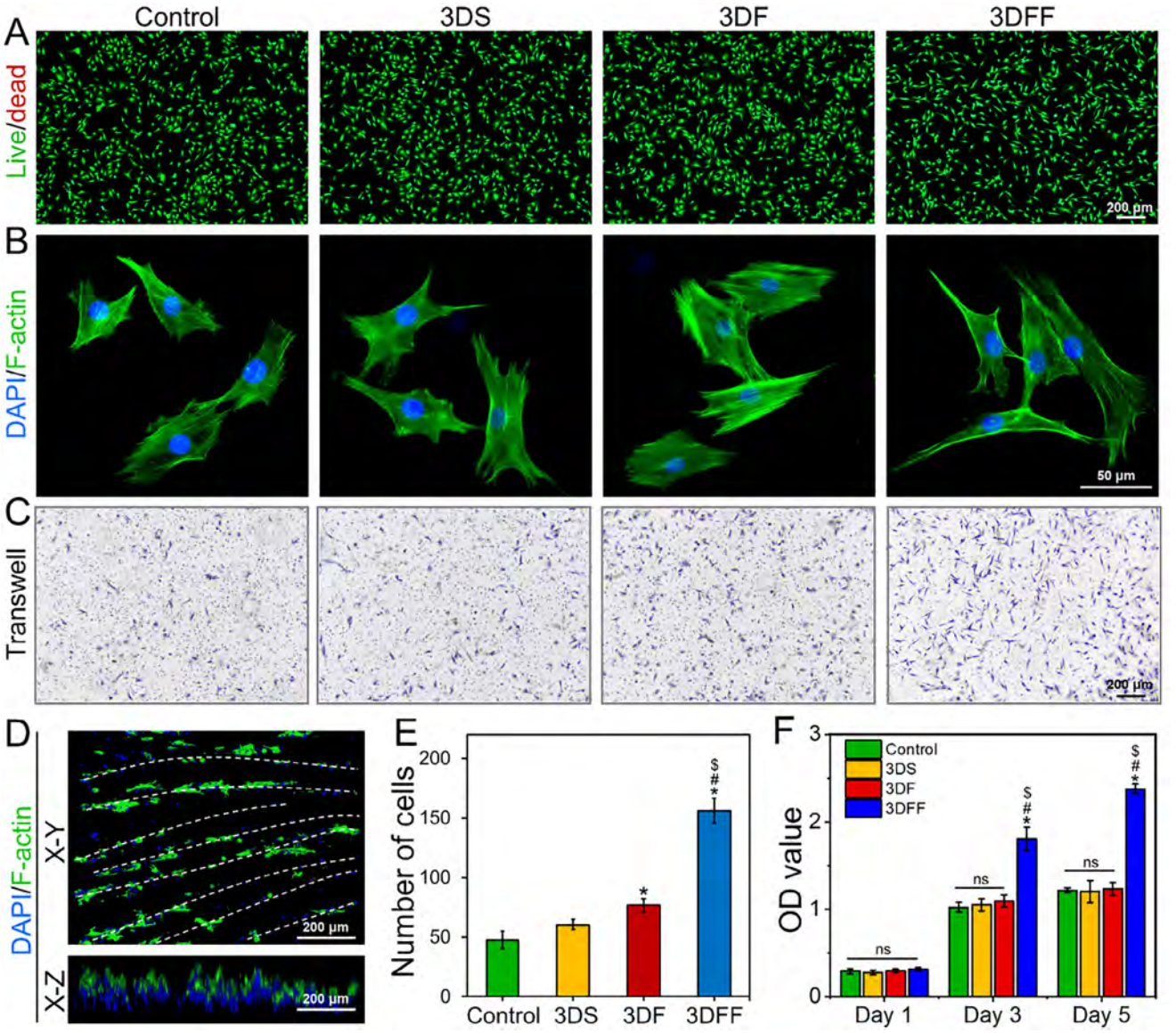

Figure 3. In vitro cytotoxicity assessment of the scaffold. A) Live/dead staining, B) DAPI/F-actin staining, and C) migration assay of AFCs after co-culturing with the extract from different scaffold for 24 h. D) The distribution of AFCs on the 3DFF scaffold after 3 d culture. The X–Y and X–Z views respectively represent the top and side perspectives, while the white lines indicate the contours of the fiber layers. E) Quantitative analysis of transwell migration assays ($n = 3$). F) CCK-8 assays of AFCs co-cultured with different scaffold extracts ($n = 3$). (*, #, $ indicate $p < 0.05$ compared to control, 3DS and 3DF, respectively.).

matrix secretion, potentially through the sustained release of bFGF.

RNA-seq was utilized to investigate DEGs in AFCs cultured for 3 days in 3DS (designated as the control group) and 3DFF. PCA demonstrated good reproducibility among replicates (**Figure** 5A). A volcano plot revealed significant differences in gene expression between the control and 3DFF groups (Figure 5B). The expression patterns of DEGs were visualized via a heatmap (Figure 5C). The results indicated that in the 3DFF group compared to the control group, the matrix synthesis-related gene Cdh11 was upregulated, while genes associated with ECM catabolism (Plau, Hyal1) and the pro-inflammatory gene Cxcl16 were significantly downregulated. Additionally, 3DFF downregulated the expression of the Apc gene in the Wnt pathway. Apc forms a complex with β-catenin, Axin, and glycogen synthase kinase 3β (GSK3β) to promote β-catenin phosphorylation, leading to its degradation and thereby inhibiting Wnt signaling. When Apc is downregulated, β-catenin cannot be efficiently phosphorylated, resulting in its cytoplasmic and nuclear accumulation, activation of downstream target genes, and promotion of cell proliferation and migration. GO functional enrichment analysis demonstrated that DEGs were primarily associated with cell migration, proliferation, locomotion and the Wnt signaling pathway (Figure 5D). KEGG pathway enrichment analysis further revealed upregulation of the Wnt signaling pathway in the 3DFF group (Figure 5E). Consistent with KEGG analysis, gene set en-

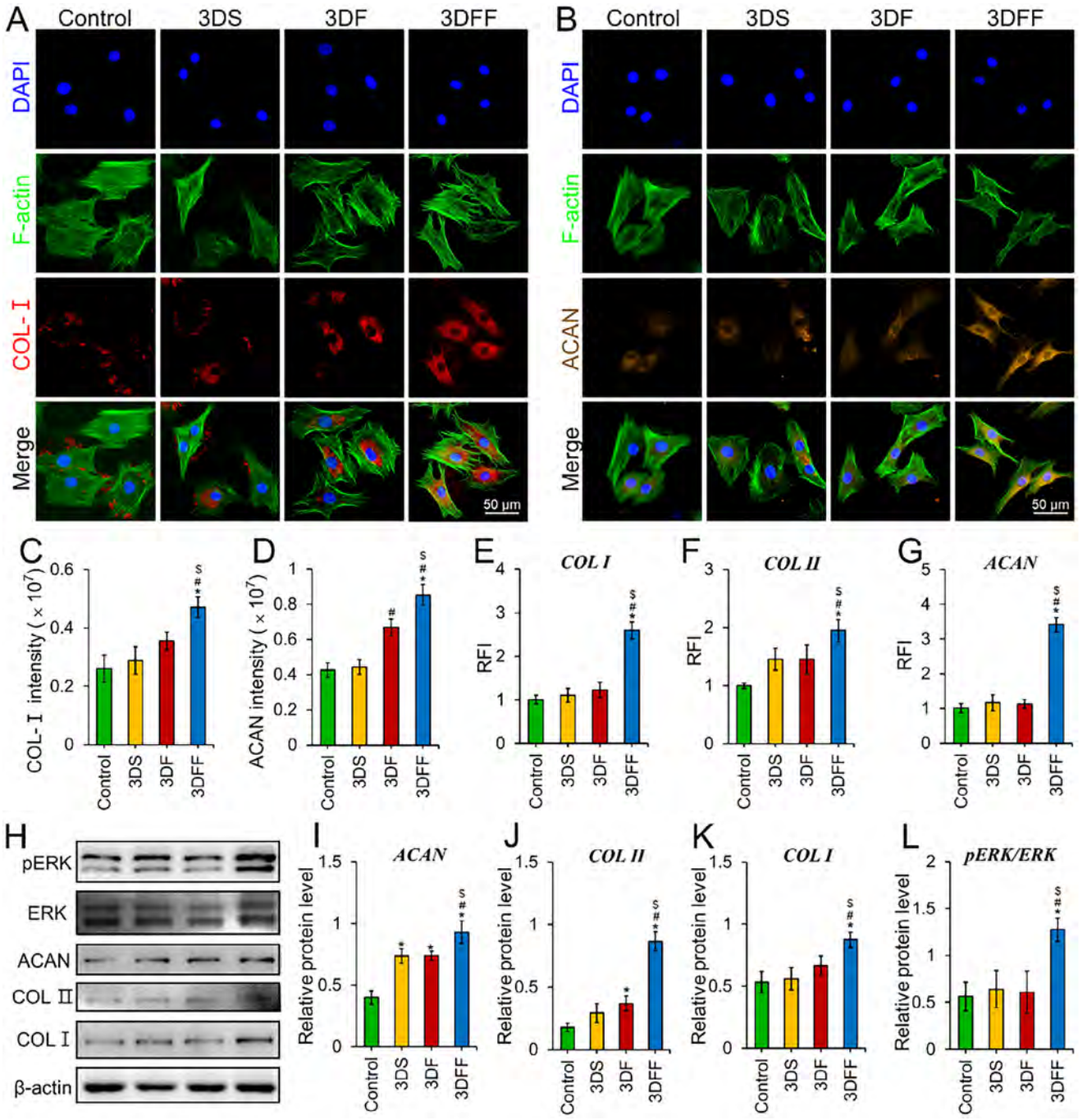

Figure 4. Matrix expression of AFCs on different scaffolds. Expression of A) COL I and B) ACAN detected by immunofluorescence staining after 5 d of co-culturing AFCs with scaffold extracts. Quantification of immunofluorescence staining for C) COL I and D) ACAN ($n = 3$). Relative mRNA expression levels of E) COL I, F) COL II, and G) ACAN in AFCs ($n = 3$). Western blot analysis of H) AFCs and quantitative analysis of I) ACAN, J) COL II, K) COL I, and L) pERK/ERK ($n = 3$). (*, #, $ indicate comparison with control, 3DS, 3DF, $p < 0.05$).

richment analysis (GSEA) demonstrated significant upregulation of the Wnt signaling pathway in the 3DFF group (Figure S2A, Supporting Information). Subsequent analysis of the Wnt pathway gene heatmap revealed downregulation of key regulators (Apc2, Axin, and GSK3β), suggesting activation of Wnt signaling pathway (Figure S2B, Supporting Information). The expression levels of the upregulated gene (Cdh11) and downregulated genes (Apc2, Cxcl16, Hyal1, and Plau) were quantitatively analyzed via qPCR. The results confirmed that the differential regulation of these genes in AFCs was consistent with the observations from the mRNA sequencing dataset (Figure 5F–J). Immunofluorescent staining demonstrated prominent nuclear translocation of β-catenin in AFCs cultured on 3DFF groups, in contrast to its predominantly membrane-bound localization in

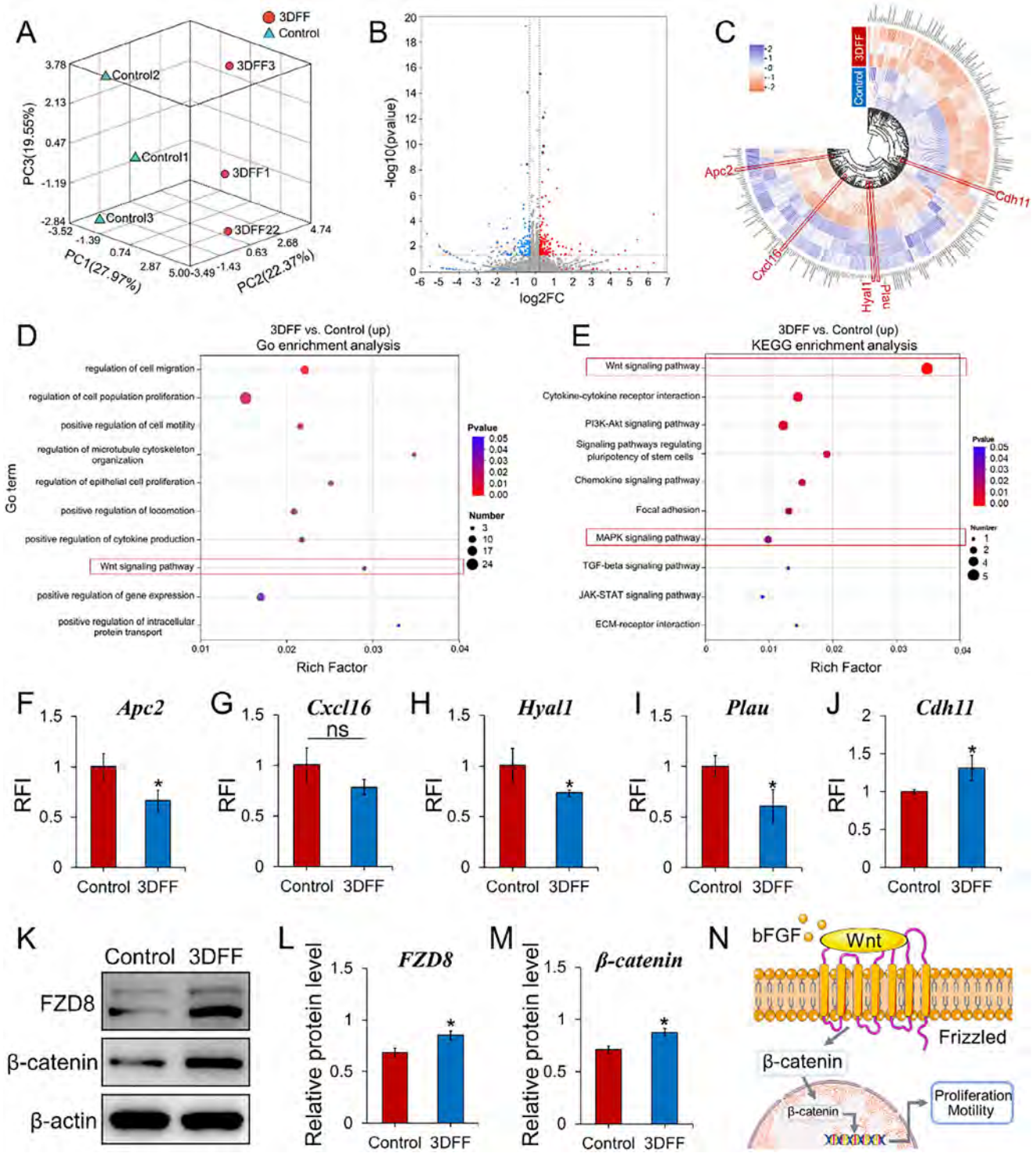

Figure 5. RNA sequencing analysis of bFGF effects on AFCs. A) Principal component analysis (PCA) of the samples. B) Volcano plot of DEGs between the 3DFF group and the control group. C) Heatmap of DEGs, where red and blue denote upregulated and downregulated genes, respectively. D) GO functional enrichment analysis of DEGs. E) KEGG analysis of DEGs. F–J) The mRNA expression levels of the selected relevant genes from the heatmap were analyzed and quantitatively detected using qPCR. K) WB analysis of AFCs in the control and 3DFF groups. L,M) Semi-quantitative assessment of protein expression performed using ImageJ software. N) Schematic representation of Wnt/β-catenin pathway activation by bFGF. (*, #, $ indicate comparison with control, 3DS, 3DF, $p < 0.05$).

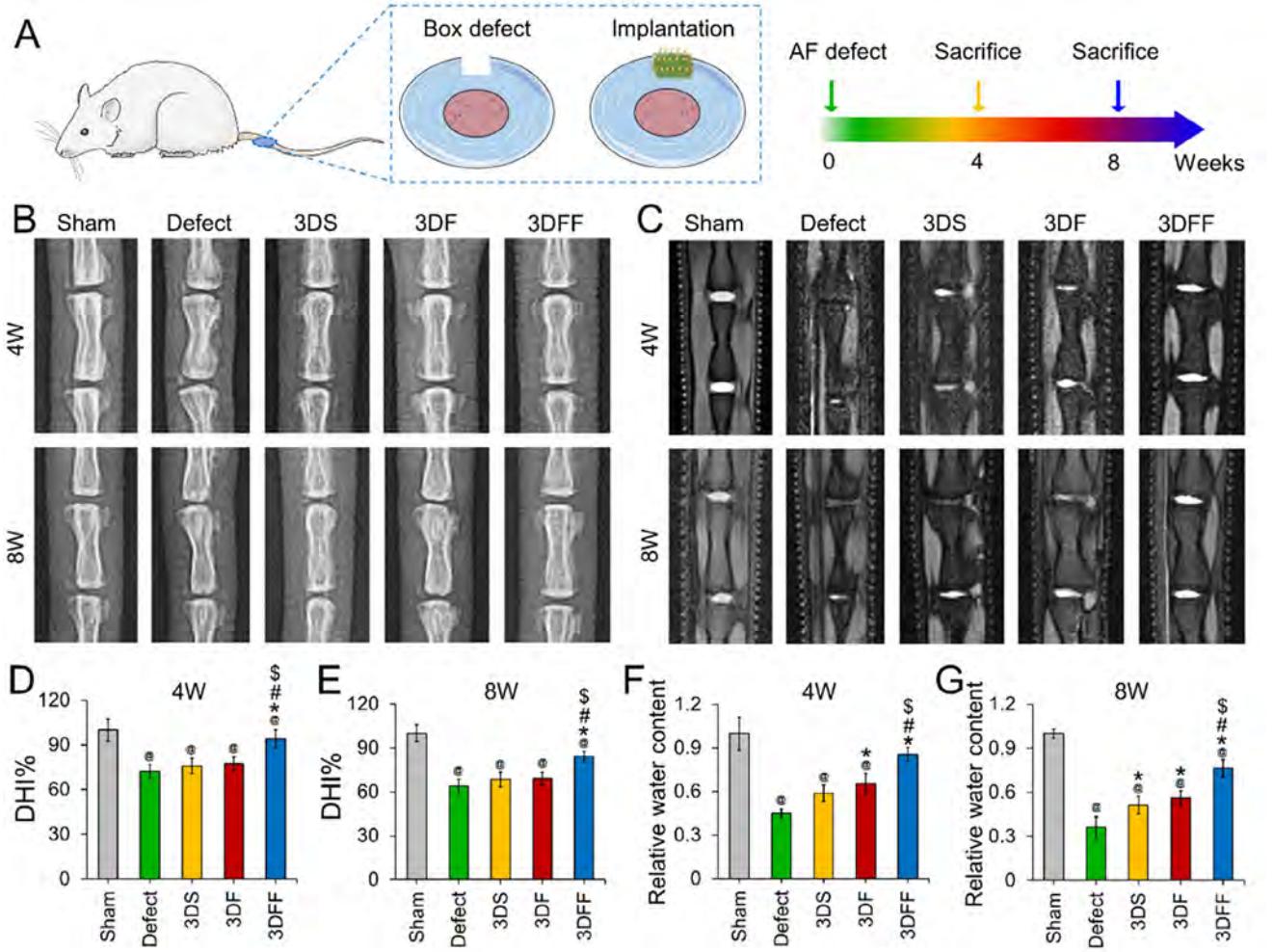

Figure 6. In vivo performance of scaffolds in repairing AF defects. A) Schematic diagram of defect model construction and scaffold implantation. B) X-ray and C) MRI images of the rat IVD at 4 and 8 weeks post-operation. Quantitative analysis of DHI at D) 4 weeks and E) 8 weeks post-operation ($n = 3$). Quantitative analysis of relative IVD water content at F) 4 weeks and G) 8 weeks post-operation (n = 3). (@, *, #, $ indicate comparison with sham, defect, 3DS, 3DF, $p < 0.05$).

control groups (Figure S3A, Supporting Information). WB analysis revealed that the 3DFF group exhibited significantly increased expression levels of FZD8 and β-catenin compared to the control group (Figure 5K–N). 3DFF scaffold downregulated Axin and GSK3β expression while reducing p-β-catenin levels (Figure S3B, Supporting Information). Furthermore, these findings collectively suggested that the 3DFF scaffold activated the Wnt/β-catenin signaling pathway, thereby enhancing the proliferation, chemotaxis, and motility of AFCs.

The in vivo efficacy of the scaffold for AF repair was investigated utilizing a rat tail IVD defect model (**Figure 6A**). Radiographic assessment of IVD height and MRI evaluation of NP signal intensity were performed at 4 and 8 weeks postoperatively (Figure 6B,C). In comparison to the sham group (4 weeks: 100.0 ± 5.7%, 8 weeks: 100.0 ± 7.6%), the defect group demonstrated a statistically significant decrease in disc height at both time points (4 weeks: 63.7 ± 4.8%, 8 weeks: 72.3 ± 4.5%). Although the 3DS (4 weeks: 68.4 ± 5.1%, 8 weeks: 75.8 ± 4.9%) and 3DF (4 weeks: 69.0 ± 4.3%, 8 weeks: 77.5 ± 4.5%) groups exhibited slightly elevated disc heights relative to the defect group, the 3DFF group (4 weeks: 84.3 ± 3.3%, 8 weeks: 93.9 ± 6.1%) displayed disc heights most comparable to the sham group and significantly superior to those of the other scaffold-treated groups (Figure 6D,E).

MRI signal intensity, indicative of IVD water content, was demonstrably higher in all scaffold-treated groups compared to the defect group (3DS: 4 weeks: 0.51 ± 0.06, 8 weeks: 0.59 ± 0.06; 3DF: 4 weeks: 0.65 ± 0.07, 8 weeks: 0.31 ± 0.05; defect: 4 weeks: 0.36 ± 0.07, 8 weeks: 0.45 ± 0.03). Notably, the 3DFF group exhibited the most pronounced signal intensity among the scaffold-treated groups (4 weeks: 0.76 ± 0.05, 8 weeks: 0.85 ± 0.05), approaching values observed in the sham group (4 weeks: 1.00 ± 0.03, 8 weeks: 1.00 ± 0.11) (Figure 6F,G). These results suggested that the 3DFF scaffold effectively preserved disc height and mitigated the progression of IVD degeneration.

Histological analysis was conducted to evaluate the effectiveness of AF repair among the various experimental groups. H&E staining demonstrated that in the defect group, NP tissue was completely supplanted by fibrotic tissue eight weeks post-

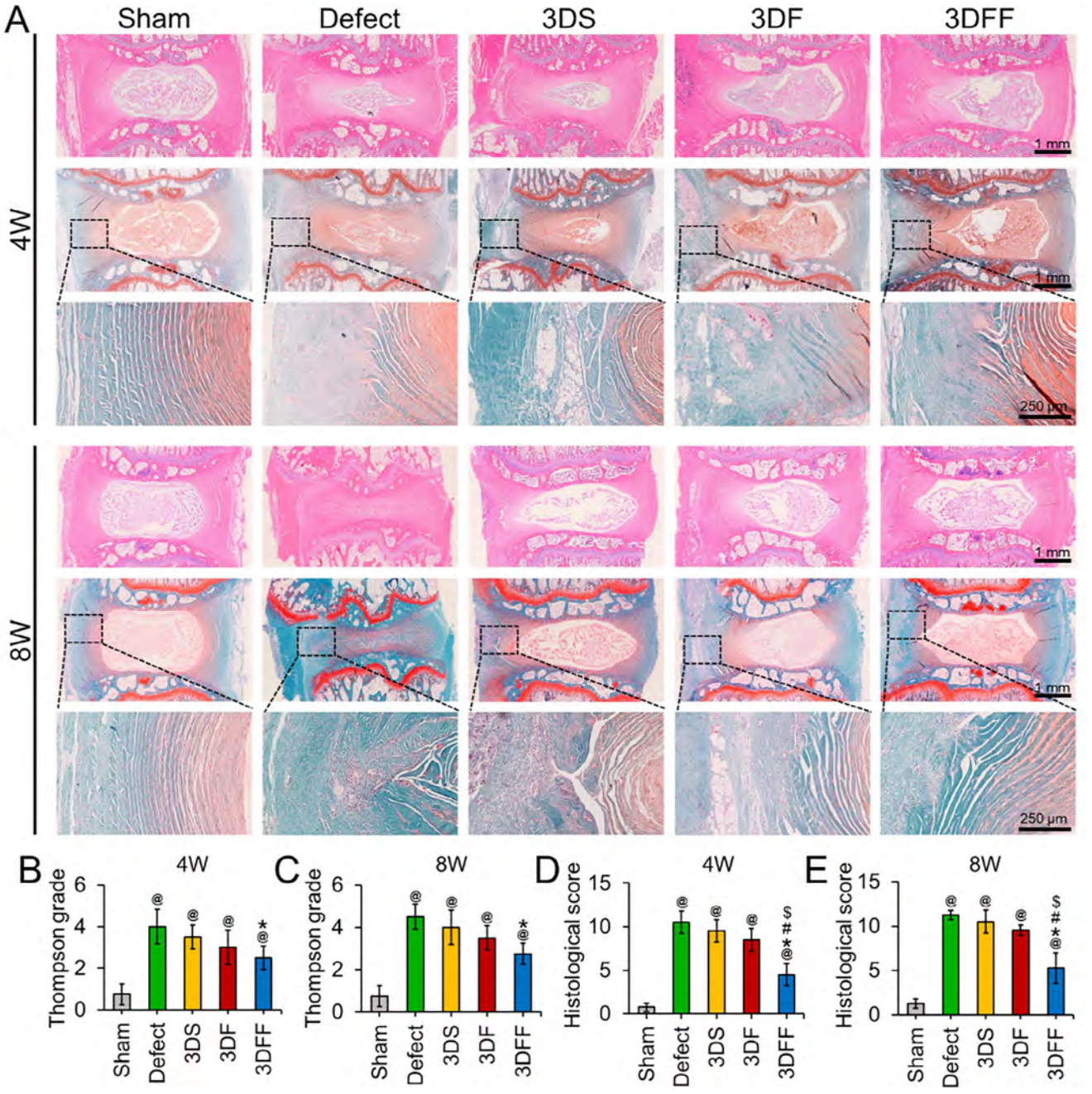

Figure 7. Histological evaluation of animal experiments. A) H&E and SO/FG staining of IVD at 4 weeks and 8 weeks. Thompson grading scores of IVD at B) 4 weeks and C) 8 weeks. Histological grading of sections from different groups at D) 4 weeks and E) 8 weeks ($n = 4$). (@, *, #, $ indicate comparison with sham, defect, 3DS, 3DF, $p < 0.05$).

operatively, and the lamellar structure of the residual AF tissue was severely disrupted (**Figure** 7A). In both the 3DS and 3DF groups, NP tissue was observed to protrude into the defect site; however, this was accompanied by conspicuous discontinuities and disorganization of the AF tissue surrounding the implant. A substantial defect area persisted within the regenerated tissue of these groups. In contrast, the 3DFF group exhibited a markedly reduced defect area, with the NP tissue retaining its rounded morphology and extending marginally into the defect site. Significantly, the architecture of the regenerated AF tissue in 3DFF group closely approximated that of the sham group.

Furthermore, the intervertebral disc tissue underwent histological grading and scoring (Figure 7B–E). The findings revealed that the 3DFF group exhibited the lowest histological grades at both 4 and 8 weeks, whereas the defect group and other experimental groups demonstrated higher grades. Specifically, the histological scores for the 3DFF group were significantly lower than those observed in the defect and other experimental groups, and

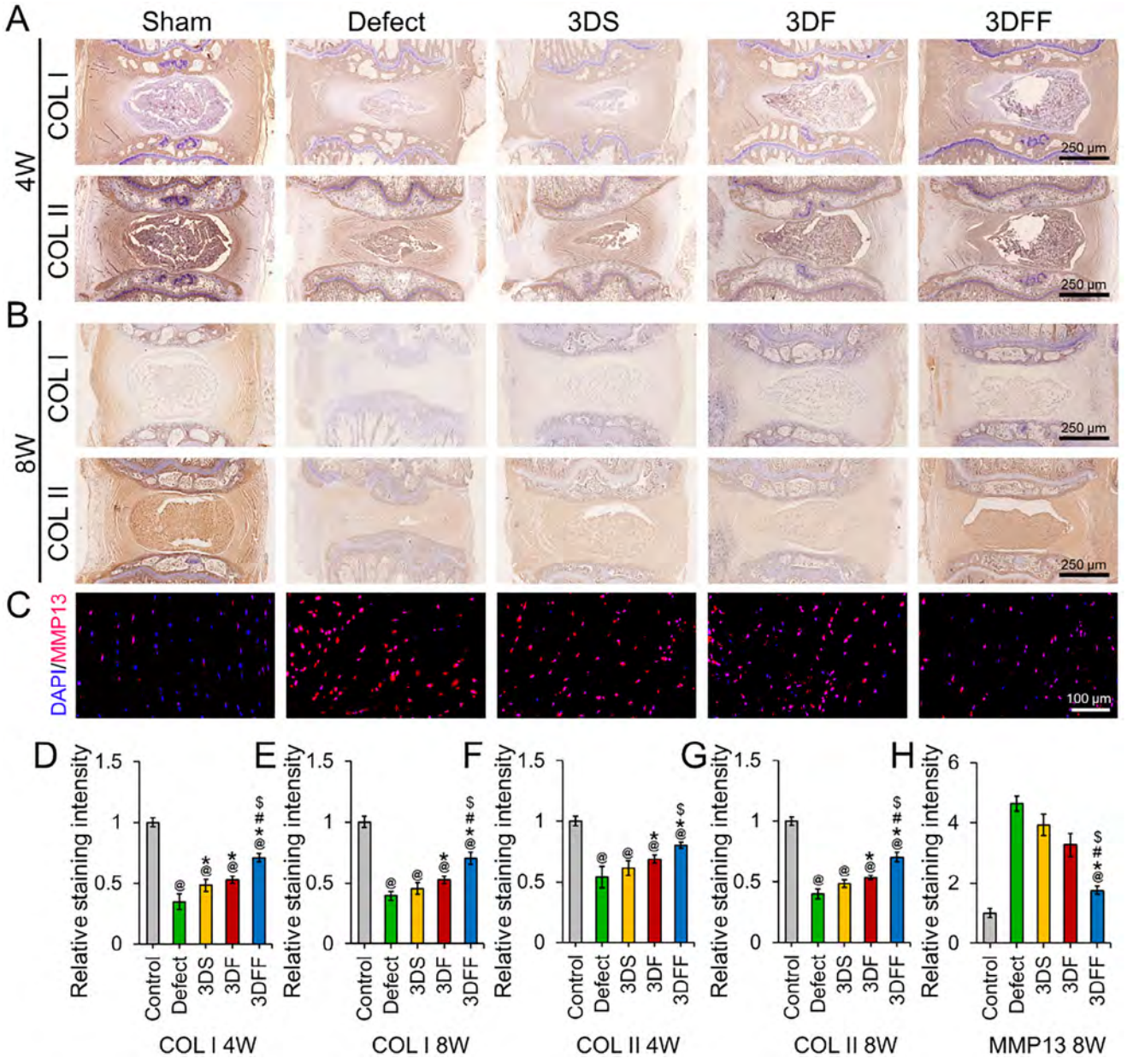

Figure 8. Immunohistochemical analysis of in vivo experiments. COL I and COL II immunohistochemical staining of IVD at A) 4 weeks and B) 8 weeks. C) MMP13 immunofluorescence staining of the annulus fibrosus at 8 weeks. Relative quantification of COL I staining intensity at D) 4 weeks and E) 8 weeks, COL II staining intensity at F) 4 weeks and G) 8 weeks, and H) relative fluorescence intensity of MMP13 immunostaining. (@, *, #, $ indicate comparison with sham, defect, 3DS, 3DF, $p < 0.05$).

most closely approximated the scores of the sham group. Immunohistochemical analysis revealed that the 3DFF group presented the largest positive areas for COL I and COL II expression in comparison to the other three groups (**Figure** 8A,B). This observation suggested that 3DFF implantation mitigated the progression of IVD degeneration. Moreover, the 3DFF group displayed a diminished level of MMP13 expression relative to the defect and other scaffold groups, implying a reduced rate of ECM degradation (Figure 8C). This trend was further substantiated by quantitative immunohistochemical and immunofluorescence analyses (Figure 8D–H). In vivo biomechanical evaluations showed that healthy IVD can accommodate gradually increasing stress through a certain range of deformation, exhibiting an average compressive modulus of 0.95 ± 0.07 MPa (Figure S4A, Supporting Information). By contrast, the defect group displayed a markedly elevated compressive modulus of 2.00 ± 0.13 MPa. Neither the 3DS group (1.61 ± 0.14 MPa) nor the 3DF group (1.46 ± 0.09 MPa) demonstrated significant improvements, indicating compromised structural integrity (Figure S4B, Supporting Information). Although the 3DFF group showed a slightly higher compressive modulus than the sham group, the difference was not statistically significant, reaching 1.18 ± 0.06 MPa. Collectively,

these findings indicate that 3DFF progressively integrated with the host tissue and facilitating AF repair and regeneration.

3. Discussion

At present, efficacious clinical strategies for the complete remediation of AF injuries remain challenging to achieve. Current approaches include synthetic polymer meshes, acellular scaffolds, cell-based therapies, and growth factor delivery systems, each with distinct advantages and limitations.[24–26] Synthetic meshes (e.g., polycaprolactone or polyurethane) provide mechanical reinforcement but often lack bioactivity, leading to poor cellular integration and fibrous encapsulation. Acellular ECM-derived scaffolds offer biocompatibility but may degrade prematurely or fail to recruit sufficient endogenous cells for functional repair. Cell-based strategies—such as implanted AFCs or stem cells—show promise in enhancing ECM production but face challenges in cell survival, phenotype maintenance, and scalability.[27] In contrast to these methods, this study introduced a novel approach to AF scaffold fabrication, employing multilayered 3D nanofibrous scaffolds functionalized with bFGF. Unlike single-component systems, our design combines structural mimicry of native AF with bioactive signaling to address both mechanical and regenerative demands. The scaffold's porous architecture facilitated cellular adhesion and ingrowth, while sustained bFGF release effectively recruited AFCs to the injury site—a critical advantage over passive scaffolds reliant on host cell infiltration alone. Consequently, the scaffold fostered a conducive microenvironment for in situ AF regeneration by stimulating cellular proliferation and augmenting ECM deposition. These findings underscore the crucial roles of 3D structural networks and supportive microenvironments in AF tissue remodeling. Compared to existing strategies, our growth factor-modified 3D scaffold offers a synergistic solution by integrating topographical cues (mimicking AF lamellar structure) with biochemical signals (bFGF), thereby overcoming limitations of inert materials or transient growth factor effects.

The architectural configuration of biomaterial scaffolds is of paramount importance, as it furnishes both structural integrity and functional support to the encompassing cellular milieu. Electrospun nanofibers have garnered considerable attention in the realm of tissue engineering owing to their capacity to emulate the ECM.[28] Nevertheless, traditional electrospun membranes are beset by inherent limitations, including restricted thickness, dense fiber packing, and insufficient interfibrillar spacing. These constraints impede cellular infiltration and restrict cellular activity to the superficial layers of the scaffold, thereby rendering 2D membranes inadequate for recapitulating the intricate 3D architecture of the native ECM and its concomitant regenerative potential. To surmount this challenge, gas foaming has emerged as a promising post-fabrication technique for transmuting nanofiber membranes into 3D scaffolds.[29] This methodology offers distinct advantages, such as expeditious production, controllable processing parameters, and the capacity to fabricate integrated, 3D, multilayered nanofiber constructs. However, a significant proportion of gas-foamed scaffolds exhibit suboptimal mechanical characteristics and bioactivity. This investigation demonstrated that gas-foamed scaffolds maintained stable mechanical properties following gelatin modification and exhibited robust shape recovery after exposure to mechanical stress. Moreover, to augment biological activity, the scaffolds were supplemented with bFGF, a well-characterized growth factor known to stimulate cellular migration and proliferation via the ERK pathway.[30,31] Our findings indicated that the incorporation of bFGF into 3D gas-foamed scaffolds enhanced ERK phosphorylation levels, thereby influencing the proliferative and migratory capacity of AFCs.

To further elucidate the molecular mechanism by which bFGF regulated AFCs function, we performed RNA sequencing analysis of AFCs with/without bFGF stimulation. KEGG pathway analysis revealed significant enrichment of the Wnt signaling pathway, with Apc identified as a key molecule mediating bFGF regulation of AFCs function. When Wnt ligands bind to frizzled receptors, GSK3β activity is inhibited, leading to increased β-catenin stability and cytoplasmic accumulation. Excess β-catenin subsequently translocates to the nucleus, where it binds with the transcriptional activator T-cell factor (TCF)/lymphoid enhancer factor (LEF) to initiate target gene transcription.[32] In cells expressing Apc, this protein forms complexes with β-catenin, Axin, and GSK3β, facilitating GSK3β-mediated phosphorylation of β-catenin. Phosphorylated β-catenin is then degraded through the proteasome-dependent pathway. When mutant Apc loses its β-catenin binding capacity, this leads to nuclear accumulation of β-catenin and activation of TCF/LEF-mediated transcription (e.g., c-myc, cyclin D1), driving cell proliferation.[33] Overexpression of Apc can inhibit cell cycle progression from G0/G1 to S phase. Furthermore, Apc participates in cell motility regulation through microtubule binding and activation of the guanine nucleotide exchange factor (Asef).[34] The Wnt pathway emerged as an enriched pathway in both GO and KEGG analyses. Biologically, Wnt activation plays a key role in tissue remodeling by regulating ECM synthesis (e.g., collagen), which is essential for annulus fibrosus homeostasis and repair.[35] Additionally, non-canonical Wnt signaling (e.g., Wnt5a) influences cell motility through cytoskeletal reorganization, potentially modulating bFGF-driven cell migration.[36] Emerging evidence also points to Wnt-FGF crosstalk in fibrogenic responses, highlighting their dichotomous roles—fibrotic (when suppressed) versus regenerative (when activated).[37] This aligns with Wnt's broader context in ECM remodeling and FGF's interplay with cell motility, as noted above. Furthermore, the upregulated KEGG pathways—ECM-receptor interaction, focal adhesion, MAPK/ERK, and PI3K-Akt—collectively drive enhanced matrix deposition through interconnected mechanisms. Integrin-mediated signaling (e.g., via FAK/Rho GTPases in ECM-receptor interaction and focal adhesion) directly activates ECM synthesis (e.g., collagen, fibronectin) and crosslinking, while focal adhesion dynamics spatially organize deposited matrix by modulating cytoskeletal tension.[38,39] Concurrently, the MAPK/ERK pathway, stimulated by growth factors, phosphorylates transcription factors like c-Jun to amplify ECM gene expression (e.g., COL1A1, FN1) and suppress matrix-degrading enzymes.[40,41] The PI3K-Akt pathway further reinforces this process by enhancing translational efficiency of ECM proteins via mTORC1 and inhibiting autophagy-mediated ECM breakdown, ensuring matrix accumulation.[42] Together, these pathways form a synergistic network that robustly promotes ECM remodeling, consistent with our transcriptomic findings. According to current research, the Wnt/β-catenin signal-

ing pathway regulates cell proliferation, differentiation, and ECM synthesis, which are key processes for effective IVD regeneration. Activation of Wnt signaling can promote the proliferation of NP cells and enhance ECM production, thus contributing to the restoration of IVD structure and function.[43] However, excessive or dysregulated activation may lead to increased cell senescence, apoptosis, and ECM degradation, which hampers regeneration and may accelerate degeneration.[44] Moreover, in the context of 3D scaffolds, the Wnt pathway mediates cellular responses to the scaffold microenvironment, influencing cell fate decisions and matrix remodeling. For example, some studies have demonstrated that moderate activation of Wnt/β-catenin signaling improves NP cell survival and ECM synthesis under mechanical stress, which is a typical condition after scaffold implantation.[45] Additionally, the non-canonical Wnt pathways, such as Wnt5a signaling, have been shown to suppress inflammation-driven degeneration and support ECM homeostasis in NP cells, further facilitating tissue repair.[46] These findings suggest that precise regulation of Wnt signaling is critical for successful NP/AF healing and regeneration following 3D scaffold implantation.[47] Future scaffold designs may benefit from incorporating modulators of the Wnt pathway to optimize regenerative outcomes.

In addition to providing a suitable microenvironment for AFCs adhesion, the AF scaffold should also facilitate endogenous AFCs recruitment and proliferation, which are essential aspects of tissue regeneration. bFGF is a potent growth factor that has been shown to promote AFCs proliferation and stimulate the proliferation, self-renewal, and differentiation of mesenchymal stem cells into fibroblasts.[48,49] A significant challenge in tissue engineering is the effective delivery of growth factors. While crucial for tissue regeneration, these biomolecules are inherently limited by their instability, short half-life, and rapid inactivation under physiological conditions. Immobilizing growth factors onto preformed 3D nanofiber scaffolds, via covalent bonding or electrostatic interactions, offers a promising strategy.[50–52] This approach circumvents exposure to harsh organic solvents and minimizes losses during processing. Furthermore, incorporating ECM proteins, such as Fn, enables direct binding to growth factors, creating a protective reservoir for controlled release and mitigating enzymatic degradation.[53] Importantly, ECM-bound growth factors retain their receptor-binding capacity, ensuring sustained and localized signaling within the matrix. This strategy enhances long-term communication between the matrix and factor receptors.[54] In this study, Fn was selected as an ECM ligand due to its ability to bind both gelatin, a common scaffold material, and various growth factors.[55,56] Fn-immobilization maintained scaffold modulus and exhibited a strong affinity for stem/progenitor cells. Previous research has indicated that the heparin-binding domain of Fn can immobilize growth factors via electrostatic interactions,[19] potentially elucidating the sustained release mechanism of bFGF.

The 3DFF scaffold exhibited superior therapeutic efficacy in the AF repair. The intrinsic 3D architecture of these scaffolds facilitated enhanced integration with the native ECM, while the sustained release of bFGF promoted endogenous cellular recruitment and subsequent matrix deposition. However, current research is not without its limitations. Specifically, the heterogeneous collagen composition of native AF tissue, characterized by distinct expression profiles within the NP and outer annulus layers, necessitates the development of scaffolds capable of recapitulating these compositional gradients and modulating matrix secretion accordingly. Furthermore, mitigating the inflammatory microenvironment following AF injury and ensuring that scaffolds provide a microenvironment conducive to the viability and physiological function of recruited cells remain critical challenges. Further investigation, encompassing long-term, large-scale animal studies, particularly those employing large animal models, is imperative to ascertain the long-term efficacy and safety of this therapeutic strategy. The establishment of reproducible AF defect models that accurately reflect clinically relevant scenarios is also of paramount importance. Finally, optimization of scaffold parameters, including bFGF concentration, fiber diameter, and porosity, is essential to address the inherent challenges associated with clinical translation.

4. Conclusion

In conclusion, this study has elucidated a highly efficacious strategy for AF regeneration, employing 3D gas-foamed nanofiber scaffolds functionalized with bFGF. This innovative approach presents a comprehensive solution to the complexities of AF repair by virtue of its provision of a biomimetic 3D microenvironment, facilitation of sustained therapeutic growth factor delivery, and stimulation of endogenous regenerative mechanisms. Continued investigation and refinement of this technology possess considerable potential to advance this therapeutic modality toward clinical implementation for individuals afflicted with debilitating IVD degeneration.

5. Experimental Section

Preparation of 2D Nanofiber Mats (2DS): PCL (10 wt%, molecular weight $Mw = 80$ kDa, Sigma-Aldrich) and Pluronic F-127 (0.5 wt%, Sigma-Aldrich) were dissolved in a mixture consisting of 10 mL dichloromethane (DCM) and N,N-dimethylformamide (DMF) at a volume ratio of 4:1. The resultant solution was then loaded into a 10 mL syringe equipped with a 20G blunt needle, and delivered at a constant rate of 3 mL/h. The electrospinning process, carried out at an applied voltage of 12 kV. The resulting 2DS was collected on aluminum foil and further processed by cutting into rectangles, followed by immersion in a sodium borohydride ($NaBH_4$) aqueous solution (0.5 M, Sinopharm Chemical Reagent Co., Ltd, Shanghai, China) for 30 min to obtain an expanded scaffold. The expanded scaffold was then treated with gelatin solution (0.5 wt%, Sigma-Aldrich) for 0.5 h to obtain 3D nanofiber scaffold (3DS). For Fn modification, the 3DS was incubated in Fn solution (2 µg mL^{-1}, YeasenBiotech) for 1 h and freeze-drying, yielding the Fn-modified scaffold (3DF). To prepare the growth factor-loaded scaffold (3DFF), recombinant rat bFGF (1 µg mL^{-1}, APEBio) was introduced onto the 3DF and incubated for 4 h prior to freeze-drying. Due to the high porosity and multilayered structure of the gas-foamed scaffold, the introduced bFGF could efficiently permeate and bind to the entire scaffold (internal and surface regions) during the 4-hour incubation, ensuring uniform growth factor distribution.

Characterization: The morphology of scaffold was examined using scanning electron microscopy (SEM). Prior to imaging, samples were sputter-coated with gold for 60 s. Interlayer spacing was measured from SEM images using Image J software. Scaffold porosity was evaluated via the liquid displacement method. Functional group analysis was conducted using Fourier-transform infrared spectroscopy (FTIR).

The release kinetics of bFGF from the 3DFF scaffold were assessed. Supernatants were collected at predetermined time intervals and the concentration of bFGF was quantified using a rat bFGF ELISA kit (Yuanchuang

Biotechnology, Shanghai, China) according to the manufacturer's instructions. Mechanical properties were determined using a mechanical testing machine. Compression tests were performed on 3DS, 3DF, and 3DFF scaffolds at a constant rate of 5 mm min^{-1}. Tests were halted upon reaching 50% strain. The compressive modulus was calculated from the resulting stress-strain curve. To assess the tensile mechanical properties of the scaffolds, rectangular specimens of 3DS, 3DF, and 3DFF (length × width × thickness: 40 mm × 10 mm × 3 mm) were prepared and clamped between grips. Uniaxial tensile tests were performed at a constant crosshead speed of 1 mm/min until failure. The specific brand and origin of the testing machine can be found in Table S1 of the Supporting Information.

Cytocompatibility of Scaffolds In Vitro: AFCs were harvested from the tails of 12-week-old male Sprague Dawley (SD) rats. Following careful removal of surrounding muscle and ligament tissue, the NP was extracted, and the remaining AF tissue was minced. The minced tissue was digested in Dulbecco's modified Eagle medium/nutrient mixture F-12 (DMEM/F12) supplemented with 150 U mL^{-1} collagenase I and 150 U mL^{-1} collagenase II for 4 h. The resulting cell suspension was centrifuged, and the isolated AFCs were cultured in DMEM/F12 supplemented with 10% fetal bovine serum (FBS), 100 U mL^{-1} penicillin, and 100 µg mL^{-1} streptomycin. Third-passage AFCs were used for all subsequent experiments.

For the cytotoxicity evaluation of the scaffolds, AFCs were seeded at a density of 5×10^4 cells per well in a 24-well plate. The cells were co-cultured with extracts from the 3DS, 3DF, and 3DFF scaffolds for 24 h. The scaffold extracts were prepared by suspending them at a concentration of 1 mg mL^{-1} in the culture medium for one week. The supernatant was then collected for cell culture. Live/dead assay was performed to assess the viability of cells. A control group was included where cells were cultured in the medium without scaffold extracts.

To assess the impact of scaffold on cell behavior, AFCs were cultured with extracts or on 3DFF for 3 days. Cell morphology and distribution were visualized using DAPI/phalloidin staining (Invitrogen, Thermo Fisher Scientific). Chemotactic response to the scaffold was evaluated using a transwell migration assay. AFCs were serum-starved overnight and seeded onto Transwell inserts (Corning) at a density of 5×10^4 cells per insert. The lower chamber contained scaffold extract. After 8 h, cells were fixed with 4% paraformaldehyde (PFA) and stained with crystal violet. Migrated cells on the underside of the insert membrane were counted. Cell proliferation was assessed using a CCK-8 assay (Beyotime, China). AFCs were cultured with scaffold extracts for 1, 3, and 5 d, and absorbance measurements were used to evaluate proliferation.

To assess ECM secretion, AFCs were cultured with extracts for 5 d, fixed, and blocked with 5% bovine serum albumin for 1 h. Immunofluorescent staining was performed using primary antibodies against collagen I (COL I, 1:200, 14695-1-AP, Proteintech), Aggrecan (ACAN, 1:200, 13880-1-AP, Proteintech) and β-catenin (1:500, 66379-1-Ig, Proteintech) at 4 °C overnight. Cells were then incubated with corresponding fluorescent secondary antibodies for 1 h and counterstained with Phalloidin and DAPI for 30 min. Finally, confocal microscopy was used for imaging.

To assess mRNA expression, AFCs were seeded at a density of 2×10^5 cells per well in six-well plates and cultured with scaffold extracts for 5 days. Total RNA was then extracted, and reverse transcription was performed using the PrimeScript RT kit (TaKaRa, Japan) to synthesize complementary DNA (cDNA). Quantitative polymerase chain reaction (qPCR) was subsequently conducted using the primer sequences listed in Table S2 (Supporting Information). The expression levels of COL I, collagen II (COL II), and ACAN were measured, with β-actin serving as the reference gene. Relative expression levels were determined using the $2^{-\Delta\Delta CT}$ method.

For protein expression analysis, AFCs were seeded at a density of 2×10^5 cells per well in six-well plates and cultured with extraction medium for 5 d. Total protein was extracted using RIPA lysis buffer, and protein concentration was determined using a BCA protein assay kit (Thermo Scientific, USA). Proteins were separated via 10% SDS-PAGE (Epizyme) and transferred to a polyvinylidene difluoride (PVDF) membrane. After blocking with skim milk, the membrane was incubated overnight with primary antibodies: COL I (1:2000, 66761-1-Ig, Proteintech), COL II (1:1000, A19308, ABclonal), ACAN (1:1000, A11691, ABclonal), ERK (1:2000, 11257-1-AP, Proteintech), pERK (1:1000, 28733-1-AP, Proteintech), FZD8 (1:1000, A18393, ABclonal), β-catenin (1:5000, 66379-1-Ig, Proteintech), Axin2 (1:5000, 20540-1-AP, Proteintech), GSK3β (1:5000, 82061-1-RR, Proteintech), and phospho-β-catenin (1:5000, 80067-1-RR, Proteintech), followed by a one-hour incubation with corresponding secondary antibodies. Chemiluminescent imaging was performed using the Tanon-5200 imaging system (Tanon, Shanghai, China). Semi-quantitative protein expression analysis was performed using Image J.

AFCs were seeded into 3DS (control group) and 3DFF extraction medium and cultured for 3 days, with three parallel samples per group. RNA was extracted from AFCs using TRIzol reagent (Invitrogen, USA). The RNA sequencing was conducted by Shanghai Majorbio Bio-pharm Biotechnology Co., Ltd., following Illumina protocols. Total RNA (1 µg) underwent polyA-selection using oligo(dT) beads, fragmentation, and double-stranded cDNA synthesis with random hexamer primers (SuperScript kit, Invitrogen). Libraries were prepared via end-repair, phosphorylation, and size selection (300 bp fragments) on agarose gel, followed by 15-cycle PCR amplification (Phusion polymerase). Quantified libraries were sequenced as 150-bp paired-end reads on NovaSeq X Plus. Raw reads were processed using fastp for quality control, then aligned to the reference genome via HISAT2. Transcript assembly and quantification utilized StringTie and RSEM, respectively. Differential expression analysis employed DESeq2 (FDR≤0.05) or DEGseq (FDR≤0.001) with $|\log2FC|\geq1$ thresholds. Functional enrichment analysis of differentially expressed genes (DEGs) included Gene Ontology (GO) terms (Goatools) and Kyoto Encyclopedia of Genes and Genomes (KEGG) pathways (KOBAS), applying Bonferroni-corrected $P \leq 0.05$ significance. All steps adhered to standardized Illumina protocols for stranded mRNA library preparation and bioinformatics pipelines. This integrated approach enabled comprehensive transcriptome profiling, quantitative gene expression analysis, and pathway characterization.

In Vivo AF Repair Assessment: Eight-week-old male Sprague-Dawley (SD) rats (average weight: 300 g) were obtained from Shanghai Regenda Co., Ltd. All experimental procedures were approved by the Ethics Committee of Shanghai Tongren Hospital (A2023-050-01). Animals were anesthetized via intraperitoneal injection of 2% sodium pentobarbital. Following aseptic preparation, a superficial defect (2.0 mm length × 1.0 mm width × 0.5 mm depth) was created in the outer AF using a surgical blade, preserving the inner AF layer to avoid damage to the nucleus pulposus. Defect dimensions were standardized by exposing the AF surface, followed by controlled partial-thickness excision guided by visual and tactile feedback. The depth was calibrated to approximately 50% of the total AF thickness. Subsequently, 3DS, 3DF, or 3DFF scaffolds, sized to match the defect, were implanted. The surgical site was closed with sutures. Animals were euthanized at 4 and 8 weeks post-implantation.

Rat tail specimens were scanned using a VDR-1800 Digital Veterinary X-ray System (Suzhou Weiterui Medical Equipment Co., Ltd.) to evaluate disc height index (DHI). DHI was calculated following the standardized protocol in IVD research, defined as the ratio of the average anterior, middle, and posterior IVD heights to the average height of adjacent vertebral bodies,[24] consistent with established methodologies in the field.[57–59] For hydration assessment, T2-weighted magnetic resonance imaging (MRI) of the central sagittal plane was performed using a 9.4T MRI scanner (Bruker BioSpin, Germany). The grayscale values of the NP were quantified using Image J software, with relative water content derived by normalizing NP signal intensity to intact discs.[2,60,61] This approach minimized inter-specimen variability.

Following imaging, rat tail samples were fixed in 4% PFA, decalcified, embedded, and sectioned. Sections underwent histological staining with hematoxylin and eosin (H&E), Safranin O-Fast Green (SO/FG), and immunohistochemistry for COL I and COL II, while MMP13 was examined using immunofluorescence. Furthermore, the repaired intervertebral disc tissue also underwent histological grading and scoring. The grading and scoring standards can be found in Tables S3 and S4 in Supporting Information. To evaluate the biomechanical properties of IVD, axial compression testing was performed. Following the removal of surrounding soft tissues from rat tails, vertebral-IVD-vertebral motion segments were care-

fully isolated. The specimens were then securely mounted in testing fixtures and subjected to compression testing at a constant displacement rate of 0.2 mm min^{-1}.

Statistical Analysis: Data are presented as mean ± standard deviation (SD). One-way ANOVA followed by Tukey's post hoc test was used to assess statistically significant differences between groups. Differences were considered statistically significant at $p < 0.05$.

Supporting Information

Supporting Information is available from the Wiley Online Library or from the author.

Acknowledgements

Y.C., Y.L., and Z.W. contributed equally to this work. This research was supported by National Natural Science Foundation of China (No. 32200591), Science and Technology Commission of Shanghai Municipality (25ZR1401323, 22Y11912000), Research Fund of Shanghai Key Laboratory of Flexible Medical Robotics (SKLFMR-0205), Medical and Industrial Cross Research Foundation of "Star of Jiaotong University" Program of Shanghai Jiao Tong University, China (Grant No. YG2022ZD030), Laboratory Open Fund of Key Technology and Materials in Minimally Invasive Spine Surgery (2024JZWC-YBA01, 2024JZWC-ZDB01), Tongren Hospital Introduces the Talented Person Scientific Research Start Funds Subsidization Project (TR2023rc08), Tongren Talent (TRKYRC-yc202201).

Conflict of Interest

The authors declare no conflict of interest.

Data Availability Statement

The data that support the findings of this study are available from the corresponding author upon reasonable request.

Keywords

annulus fibrosus, electrospinning, gas foaming, intervertebral disc, multilayered structure

Received: June 5, 2025
Revised: August 10, 2025
Published online:

[1] J. C. Iatridis, J. Kang, R. Kandel, M. V. Risbud, *J. Orthop. Res.* **2017**, *35*, 5.
[2] K. Fujii, M. Yamazaki, J. D. Kang, M. V. Risbud, S. K. Cho, S. A. Qureshi, A. C. Hecht, J. C. Iatridis, *JBMR Plus* **2019**, *3*, 10180.
[3] M. D. Harmon, D. M. Ramos, D. Nithyadevi, R. Bordett, S. Rudraiah, S. P. Nukavarapu, I. L. Moss, S. G. Kumbar, *Biomater. Sci.* **2020**, *8*, 1216.
[4] G. Chang, H. J. Kim, G. Vunjak-Novakovic, D. L. Kaplan, R. Kandel, *J. Biomed. Mater. Res., Part A* **2010**, *92*, 43.
[5] G. Chu, C. Shi, H. Wang, W. Zhang, H. Yang, B. Li, *Front. Bioeng. Biotechnol.* **2018**, *6*, 90.
[6] G. T. Desmoulin, V. Pradhan, T. E. Milner, *Spine* **2020**, *45*, 457.
[7] Y. F. Chiang, C. J. Chiang, C. H. Yang, Z. C. Zhong, C. S. Chen, C. K. Cheng, Y. H. Tsuang, *Clin. Biomech.* **2012**, *27*, 241.
[8] W. J. Choy, K. Phan, A. D. Diwan, C. S. Ong, R. J. Mobbs, *BMC Musculoskeletal Disord.* **2018**, *19*, 290.
[9] Y. Wan, G. Feng, F. H. Shen, C. T. Laurencin, X. Li, *Biomaterials* **2008**, *29*, 643.
[10] X. Xie, Y. Chen, X. Wang, X. Xu, Y. Shen, A. Ur. R. Khan, A. Aldalbahi, A. E. Fetz, G. L. Bowlin, M. El-Newehy, X. Mo, *J. Mater. Sci. Technol.* **2020**, *59*, 243.
[11] Y. Chen, X. Dong, M. Shafiq, G. Myles, N. Radacsi, X. Mo, *Adv. Fiber Mater.* **2022**, *4*, 959.
[12] Y. Chen, W. Xu, M. Shafiq, J. Tang, J. Hao, X. Xie, Z. Yuan, X. Xiao, Y. Liu, X. Mo, *J. Colloid Interface Sci.* **2021**, *603*, 94.
[13] Y. Chen, Z. Jia, M. Shafiq, X. Xie, X. Xiao, R. Castro, J. Rodrigues, J. Wu, G. Zhou, X. Mo, *Colloids Surf., B* **2021**, *201*, 111637.
[14] F. J. Lyu, K. M. Cheung, Z. Zheng, H. Wang, D. Sakai, V. Y. Leung, *Nat. Rev. Rheumatol.* **2019**, *15*, 102.
[15] M. Segel, B. Neumann, M. F. E. Hill, I. P. Weber, C. Viscomi, C. Zhao, A. Young, C. C. Agley, A. J. Thompson, G. A. Gonzalez, A. Sharma, S. Holmqvist, D. H. Rowitch, K. Franze, R. J. M. Franklin, K. J. Chalut, *Nature* **2019**, *573*, 130.
[16] Y. C. Huang, Y. Hu, Z. Li, K. D. K. Luk, *J. Tissue Eng. Regener. Med.* **2018**, *12*, 2188.
[17] N. Guan, Z. Liu, Y. Zhao, Q. Li, Y. Wang, *Drug Delivery* **2020**, *27*, 1438.
[18] R. Kang, D. Q. Svend Le, H. Li, H. Lysdahl, M. Chen, F. Besenbacher, C. Bünger, *J. Mater. Chem. B* **2013**, *1*, 5462.
[19] Z. Chen, Z. Lv, Y. Zhuang, Q. Saiding, W. Yang, W. Xiong, Z. Zhang, H. Chen, W. Cui, Y. Zhang, *Adv. Mater.* **2023**, *35*, 2300180.
[20] W. Zhang, Y. Wu, Q. Chen, H. Zhang, M. Zhou, K. Chen, C. Cao, H. Guo, J. Xu, H. Liu, H. Lin, C. Liu, R. Liu, *Adv. Sci.* **2022**, *9*, 2200775.
[21] K. Zhang, X. Bai, Z. Yuan, X. Cao, X. Jiao, Y. Li, Y. Qin, Y. Wen, X. Zhang, *Biomaterials* **2019**, *204*, 70.
[22] X. Xie, D. Li, Y. Chen, Y. Shen, F. Yu, W. Wang, Z. Yuan, M. Yosry, J. Wu, X. Mo, *Adv. Healthcare Mater.* **2021**, *10*, 2100918.
[23] Y. Chen, Y. Li, X. Wang, X. Mo, Y. Chen, Z. Deng, X. Ye, J. Yu, *ACS Appl. Mater. Interfaces* **2024**, *16*, 61664.
[24] Q. Wei, D. Liu, G. Chu, Q. Yu, Z. Liu, J. Li, Q. Meng, W. Wang, F. Han, B. Li, *Bioact. Mater.* **2023**, *19*, 581.
[25] S. B. G. Blanquer, D. W. Grijpma, A. A. Poot, *Adv. Drug Delivery Rev.* **2015**, *84*, 172.
[26] Y. Peng, X. Chen, Z. Rao, W. Wu, H. Zuo, K. Chen, K. Li, H. Lin, S. Liu, Y. Xiao, B. Wang, D. Quan, X. Qing, Y. Bai, Z. Shao, *Acta Biomater.* **2023**, *170*, 288.
[27] J. Schol, D. Sakai, *Int. Orthop.* **2019**, *43*, 1011.
[28] T. Huang, Y. E. Zeng, C. Li, Z. Zhou, J. Xu, L. Wang, D. G. Yu, K. Wang, *ACS Biomater. Sci. Eng.* **2024**, *10*, 4114.
[29] M. Kamaraj, N. Moghimi, J. Chen, R. Morales, S. Chen, A. Khademhosseini, J. V. John, *Trends Biotechnol.* **2024**, *42*, 631.
[30] S. Guo, L. Yu, Y. Cheng, C. Li, J. Zhang, J. An, H. Wang, B. Yan, T. Zhan, Y. Cao, H. Zheng, Z. Li, *Cell Biol. Int.* **2012**, *36*, 945.
[31] H. Pratsinis, D. Kletsas, *Eur. Spine J.* **2007**, *16*, 1858.
[32] E. S. Blomain, J. A. Rappaport, A. M. Pattison, B. Bashir, E. Caparosa, J. Stem, A. E. Snook, S. A. Waldman, *Cancer Biol. Ther.* **2020**, *21*, 441.
[33] A. M. Ashmawy, K. M. Elgeshy, E. S. T. Abdel Salam, M. Ghareeb, M. H. Kobaisi, H. A. A. Amin, S. K. Sharawy, A. H. A. Abdel Wahab, *Arab. J. Gastroenterol.* **2017**, *18*, 144.
[34] T. Senda, A. Shimomura, A. Iizuka-Kogo, *Anat. Sci. Int.* **2005**, *80*, 121.
[35] Z. Zhou, P. Song, Y. Wu, M. Wang, C. Shen, Z. Ma, X. Ren, X. Wang, X. Chen, Y. Hu, Z. Li, Q. Zhang, M. Li, Z. Geng, J. Su, *Mater. Horiz.* **2024**, *11*, 1465.
[36] S. Rogers, S. Scholpp, *Semin. Cell Dev. Biol.* **2022**, *125*, 3.

[37] D. L. Jones, M. P. Morley, X. Li, Y. Ying, G. Zhao, S. E. Schaefer, L. R. Rodriguez, F. L. Cardenas-Diaz, S. Li, S. Zhou, U. V. Chembazhi, M. Kim, C. Shen, A. Nottingham, S. M. Lin, E. Cantu, J. M. Diamond, M. C. Basil, A. E. Vaughan, E. E. Morrisey, *Science* **2024**, *386*, ado5561.
[38] C. Huang, M. Lei, Q. Zhong, W. Lian, T. Kang, J. Hu, *J. Cell. Physiol.* **2024**, *239*, 31359.
[39] W. Wu, X. Guo, T. Qu, Y. Huang, J. Tao, J. He, X. Wang, J. Luo, *Nutrients* **2024**, *16*, 1958.
[40] J. Yang, X. Weng, C. Chen, Y. Pan, *Discovery Med.* **2025**, *37*, 486.
[41] S. Zhu, M. Zhang, Z. Qu, S. Xu, J. Peng, F. Jiang, *J. Cell Commun. Signal.* **2025**, *19*, 12059.
[42] C. C. Dibble, L. C. Cantley, *Trends Cell Biol.* **2015**, *25*, 545.
[43] S. S. Cheon, P. Nadesan, R. Poon, B. A. Alman, *Exp. Cell Res.* **2004**, *293*, 267.
[44] A. Hiyama, D. Sakai, M. V. Risbud, M. Tanaka, F. Arai, K. Abe, J. Mochida, *Arthritis Rheum.* **2010**, *62*, 3036.
[45] Z. Li, S. Chen, S. Chen, D. Huang, K. Ma, Z. Shao, *J. Cell. Biochem.* **2019**, *120*, 12519.
[46] Z. Li, K. Zhang, X. Li, H. Pan, S. Li, F. Chen, J. Zhang, Z. Zheng, J. Wang, H. Liu, *Osteoarthritis Cartilage* **2018**, *26*, 966.
[47] Z. L. Wu, Q. Q. Xie, T. C. Liu, X. Yang, G. Z. Zhang, H. H. Zhang, *Pathol. Res. Pract.* **2021**, *220*, 153366.
[48] Z. Tu, F. Han, Z. Zhu, Q. Yu, C. Liu, Y. Bao, B. Li, F. Zhou, *Acta Biomater.* **2023**, *166*, 241.
[49] P. Gallego-Muñoz, L. Ibares-Frías, M. C. Valsero-Blanco, R. Cantalapiedra-Rodriguez, J. Merayo-Lloves, M. C. Martínez-García, *Cytokine* **2017**, *96*, 94.
[50] A. Gupta, S. Singh, *Mol. Neurobiol.* **2022**, *59*, 983.
[51] R. C. H. Gresham, C. S. Bahney, J. K. Leach, *Bioact. Mater.* **2021**, *6*, 1945.
[52] S. O. Sarrigiannidis, J. M. Rey, O. Dobre, C. González-García, M. J. Dalby, M. Salmeron-Sanchez, *Mater. Today Bio* **2021**, *10*, 100098.
[53] A. Prasad, R. A. Clark, *G. Ital. Dermatol. Venereol.* **2018**, *153*, 361.
[54] K. M. Sawicka, M. Seeliger, T. Musaev, L. K. Macri, R. A. F. Clark, *Adv. Wound Care* **2015**, *4*, 469.
[55] J. Klavert, B. C. J. van der Eerden, *Front. Bioeng. Biotechnol.* **2021**, *9*, 663357.
[56] J. Patten, K. Wang, *Adv. Drug Delivery Rev.* **2021**, *170*, 353.
[57] Y. Xu, F. Cai, Y. Zhou, J. Tang, J. Mao, W. Wang, Z. Li, L. Zhou, Y. Feng, K. Xi, Y. Gu, L. Chen, *Sci. Adv.* **2024**, *10*, ado7249.
[58] K. D. Hudson, M. Alimi, P. Grunert, R. Härtl, L. J. Bonassar, *Curr. Opin. Biotechnol.* **2013**, *24*, 872.
[59] Q. Meng, E. Xie, H. Sun, H. Wang, J. Li, Z. Liu, K. Li, J. Hu, Q. Chen, C. Liu, B. Li, F. Han, *Adv. Mater.* **2023**, *36*, 2305468.
[60] Q. Yu, F. Han, Z. Yuan, Z. Zhu, C. Liu, Z. Tu, Q. Guo, R. Zhao, W. Zhang, H. Wang, H. Mao, B. Li, C. Zhu, *Acta Biomater.* **2022**, *148*, 73.
[61] X. Yang, X. Li, *Eur. Spine J.* **2009**, *18*, 1564.